Effects of Thermal Treatment on Acoustic Waves in Carrara Marble

Matthias Ruf [1], **Holger Steeb** [1,2]

[1]University of Stuttgart, Institute of Applied Mechanics (CE), Pfaffenwaldring 7, D-70569 Stuttgart, Germany
[2]University of Stuttgart, SC SimTech, Pfaffenwaldring 5a, D-70569 Stuttgart, Germany

Key Points:

- Thermal treatments of Carrara marble lead to significant bulk volume increase which correlates with the initiated crack volume
- Influence of max. temperature (100 °C to 600 °C), cooling protocol (slow vs. fast), and sample size on acoustic wave propagation are studied
- A new model predicting the evolution of acoustic velocities is proposed based on experimentally measurable volume changes

Corresponding author: Matthias Ruf, matthias.ruf@mechbau.uni-stuttgart.de

Corresponding author: Holger Steeb, holger.steeb@mechbau.uni-stuttgart.de

Abstract

Many physical processes in the field of rock physics are influenced by the presence of fractures and microcracks. Therefore, intact rock samples are often used for reproducible experimental studies, and cracks are artificially created by various methods. For this, one possibility is the use of thermal treatments. In this work, twelve thermal treatments, differing in the applied maximum temperature and the applied cooling condition (slow versus fast cooling) are experimentally studied for dry Bianco Carrara marble under ambient conditions. Two sizes of cylindrical core samples are investigated to identify a potential size effect. As effective quantities on the core-scale, the bulk volume, the bulk density, and the P- and S-wave velocities, including shear wave splitting, are examined. To obtain a three-dimensional insight into the mechanisms occurring on the micro-scale level, micro X-Ray Computed Tomography (μXRCT) imaging is employed. For both cooling conditions, with increasing maximum temperature, the bulk volume increases, and the propagation velocities significantly drop. This behavior is amplified for fast cooling. The bulk volume increase is related to the initiated crack volume as μXRCT shows. Based on comprehensive measurements, a logarithmic relationship between the relative bulk volume change and the relative change of the ultrasound velocities can be observed. Although there is a size effect for fast cooling, the relationship found is independent of the sample size. Also the cooling protocol has almost no influence. A model is derived which predicts the relative change of the ultrasound velocities depending on the initiated relative bulk volume change.

Plain Language Summary

Many physical processes in the field of rock physics are influenced by the presence of fractures and microcracks. Therefore, intact rock samples are often used for reproducible experimental studies, and cracks are artificially created by various methods. For this, one possibility is the use of thermal treatments. In the simplest case, the samples are heated from room temperature to a maximum temperature and cooled back afterward. By varying the maximum temperature and/or the cooling condition (slow versus fast cooling), the resulting microcrack network can be manipulated. Within this work, these two possibilities are experimentally investigated for cylindrical Bianco Carrara marble core samples in a dry state under ambient conditions. The characterization of the modified microstructure is performed by ultrasound velocity measurements as well as bulk volume measurements. For understanding the mechanisms occurring in the microstructure, micro-X-ray computed tomography imaging is used to provide a non-invasive three-dimensional insight of the samples. Based on comprehensive measurements, a logarithmic relationship between the relative bulk volume change and the relative change of the ultrasound velocities can be observed. Based on this, a model is derived which predicts the relative change of the ultrasound velocities depending on the initiated relative bulk volume change.

1 Introduction

Bianco Carrara marble is a popular crystalline rock and frequently used in experimental rock physics to study different physical phenomena, cf. e.g. Peacock et al. (1994), Pieri et al. (2001), Schubnel, Walker, et al. (2006), Schubnel, Benson, et al. (2006), Delle Piane and Burlini (2008), Arena et al. (2014), Delle Piane et al. (2015), Sarout et al. (2017), Kandula et al. (2019), and Lissa et al. (2021). Reasons are its high mineral purity, consisting of 98 % calcite (Pieri et al., 2001), the low porosity of 0.7 % (Howarth et al., 1986), combined with its almost isotropic and homogeneous mechanical behavior on the macroscopic level. All resulting in a very reproducible material for experimental rock studies which was already suggested by Ramez and Murrell (1964) based on a petrofabric analysis of Carrara marble.

Carrara marble is not only used in its virgin state under ambient conditions but often modified in its microstructure by mechanical or thermal treatments. Both with the aim to initiate microfractures (microcracks). The terms microfractures and microcracks will here be used synonymously as in Anders et al. (2014) and Kranz (1983). The low porosity combined with the nearly mono-mineral composition allows the almost pure study of how microcracks affect the mechanical and hydro-mechanical properties on the macro-scale. Besides the initiation of microcracks by a mechanical load, used, for instance, in Peacock et al. (1994) for the experimental verification of Hudson's theory, the second possibility is to subject the specimens to a thermal treatment. Here, in the simplest case, the specimen is heated-up to a specific maximum temperature, which is held for a certain period until a uniform sample temperature distribution is ensured. Afterward, the sample is cooled back to room temperature. In principle, various cooling protocols are available. However, the two extreme cases are to perform the cooling very slowly, for instance, in the switched-off but still closed oven, or very fast, for instance, by quenching the samples in water. For the latter, the term thermal shock is frequently used. In both cases, the creation of microcracks can be observed. Recent developments and new investigation methods in the field of experimental rock physics have led to a renewed interest in thermal treatments for the initiation of cracks in Carrara marble, cf. Pimienta et al. (2019), Sarout et al. (2017), and Delle Piane et al. (2015). Also in other research areas dealing with the physical weathering of Carrara marble, artificially aging by thermal treatment cycles is still of interest, cf. El Boudani et al. (2015b, 2015a), and Siegesmund et al. (2000). In a recent work of Pimienta et al. (2019), among other crustal rocks, Carrara marble was investigated in regard to its elastic and electrical properties in relation to a varying degree of microfracturing. The microfracturing was achieved by applying different heat protocols (different maximum temperatures) and a slow cooling down (overnight) inside the oven. The effect of rapid cooling instead of slow cooling was not studied and no statistics were considered. Since also thermal shock is a frequently used cooling method, cf. Sarout et al. (2017), and Delle Piane et al. (2015), the question arise how the nature of the initiated cracks and their effect on the macroscopic properties differs.

The presented research explores, for the first time, as far as the authors know, the different effects of a slow cooling procedure compared to a fast cooling for dry Carrara marble under ambient conditions in a systematic approach. As maximum temperatures the range from 100 °C to 600 °C in 100 K increments is investigated. Further, the influence of the specimen size is taken into account to see if a size effect exists. For this, cylindrical core samples of two different sizes but with the same aspect ratio are investigated. To quantify how the specimens are affected by the corresponding thermal treatment on the macro-scale, the bulk volume, the bulk density, as well as P- and S-wave velocity changes are related to the properties before the thermal treatment was applied. For S-wave propagation, shear wave splitting is taken into account to see if a possible anisotropy is caused by the thermal treatments. The results are linked to the changes on the micro-scale in a phenomenological qualitative manner by employing micro X-Ray Computed Tomography (μXRCT) scans of sub-volumes of selected samples. This allows a three-dimensional insight into the modified microstructure. From the numerous characterizations, it can be followed that almost independent of the applied cooling procedure and independent of the sample size a logarithm relationship between the relative bulk volume change and the relative change of the ultrasonic velocities exists. This result is the basis of a new model predicting evolving acoustic velocities based on relative bulk volume changes. Moreover, it is discussed how the different thermal treatments are related to each other.

2 Materials and Methods

2.1 Thermal Treatments and Samples Preparation

As main geometry, cylindrical core samples with a diameter $d = 29\,\text{mm}$ and a length $l = 72.5\,\text{mm}$ were used. To study a potential size effect, a second sample size with a diameter of $d = 12\,\text{mm}$ and a length of $l = 30\,\text{mm}$ was considered. Thus, both sample geometries have an identical aspect ratio of $l/d = 2.5$. The large samples were extracted from two Carrara marble blocks with a thickness of 80 mm and the small ones from one block with a thickness of 40 mm by water-cooled diamond drilling. Drilling orientation of all samples was chosen identical. To ensure a perfect cylindrical geometry, the samples were reworked to the final size specified above employing a lathe.

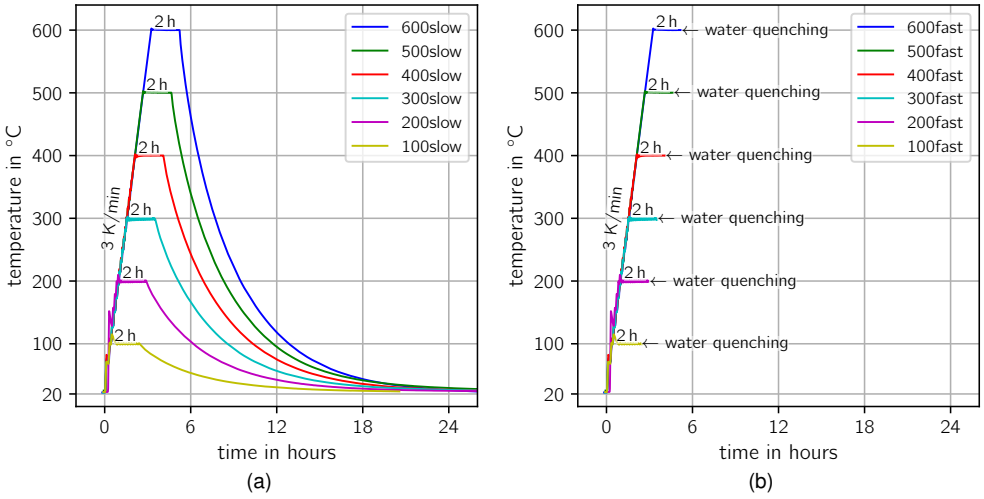

Figure 1. Illustration of the 12 studied thermal treatments based on the logged oven temperature. Investigated maximum temperatures 100 °C, 200 °C, 300 °C, 400 °C, 500 °C and 600 °C. Identical heating rate of $3\,\text{K}\,\text{min}^{-1}$ and holding time of 120 min at maximum temperature. (a) Slow cooling. (b) Fast cooling.

After the initial characterization of the untreated cores, the specimens were subjected to different thermal treatments. Treatments involve three steps:

1. Heating-up from room temperature to the maximum temperature T_{max} with a constant, relatively low heating rate to avoid bigger temperature gradients inside the samples.
2. Holding of T_{max} for a certain period to achieve a uniform temperature distribution inside the samples.
3. Cooling the samples back to room temperature ($\approx 20\,°\text{C}$) with a certain cooling protocol.

To cover the entire temperature range from room temperature up to a temperature of 600° where the decomposition of calcite significantly begins, cf. Rodriguez-Navarro et al. (2009), we used as maximum temperatures T_{max} in our study 100 °C, 200 °C, 300 °C, 400 °C, 500 °C and 600 °C. For the cooling procedures, we distinguish between the two extremes of "slow" and "fast" cooling. Slow cooling was performed in the switched-off but still closed oven and fast cooling by quenching the samples in a big water basin

filled with water at room temperature ($\approx 20\,^{\circ}\mathrm{C}$). All remaining parameters were set constant. The heating rate was set to $3\,\mathrm{K\,min^{-1}}$ and the subsequent holding time for $T_{\max}$ was set to 120 min as in Sarout et al. (2017) and Delle Piane et al. (2015). The latter ensures a uniform temperature distribution in the whole sample. It is noted, that this is a conservative value and almost after a significantly shorter holding period a uniform temperature distribution is achieved as can be shown, for instance, by a vague estimation of the characteristic thermal diffusion time. The resulting 12 different thermal treatment profiles, based on the temperature inside the furnace chamber, are shown in Figure 1. They are grouped in slow (a) and fast cooling (b) treatments. The cooling profile of slow cooling depends on the furnace insulation. At least, if the cooling rate cannot be controlled, as in our case, in the employed laboratory chamber furnace *Carbolite CWF 11/5 + 301 Controller* from Carbolite Gero GmbH & Co. KG, Germany. The highest maximum cooling gradient in amounts occurs directly after switching-off and is about $6.13\,\mathrm{K\,min^{-1}}$ for $T_{\max} = 600\,^{\circ}\mathrm{C}$. However, compared to the cooling gradient emerging in water quenching which is several orders of magnitude higher, this is extremely low, cf. Figure 9. In the following, we use the value of $T_{\max}$ in degree Celsius followed by the term "slow" or "fast", indicating the applied cooling procedure, to refer to the different thermal treatments. It should be mentioned, that a temperature overshot after the transition from the heating-up to the holding phase can be observed, cf. Figure 1. After few oscillations, the setpoint of $T_{\max}$ is finally reached. This could slightly influence the results of the samples subjected to lower maximum temperatures ($100\,^{\circ}\mathrm{C}$ and $200\,^{\circ}\mathrm{C}$) since the relative influence is here more significant.

To obtain statistical significance, three samples per thermal treatment for the large sample geometry were analyzed resulting in 36 samples. Besides, three additional samples were left untreated, which may be used for future reference purposes. For the small sample geometry, statistics were not taken into account and only one sample per thermal treatment was prepared, resulting in 12 samples for all thermal treatments. One more sample was left untreated for the same reason as for the large ones. To refer to the different samples, we use the following key: the thermal treatment, cf. Figure 1, the value of the nominal diameter in millimeter, and a continuous sample number for the specific thermal treatment. All samples were investigated in the dry state and under ambient (laboratory) conditions. Further, classical oven drying was deliberately not done to avoid any potential influence. Instead, all samples were dried for several days under ambient conditions between the different steps of the measurement workflow.

2.2 Experimental Characterization

To systematically study the effects of the different thermal treatments, each sample was characterized before and after the respective thermal treatment. All measurements were performed under ambient (laboratory) conditions. To distinguish between the moment of the measurements, we introduce the superscript "(0)" for the measurements before the thermal treatment, and the superscript "(1)" for the measurements after. In Figure 2 the measurement workflow is summarized. Their measurement and the calculation of the used derived physical quantities are described briefly in the following. For further details see Appendix A.

For the determination of the bulk volume V and the bulk density ρ, a perfect cylindrical shape of the samples was assumed. This allows to use the sample diameter d and length l to calculate the bulk volume given by $V = (\pi/4)d^2 l$. Together with the sample mass m, the bulk density follows by $\rho = m/V$. The underlying diameter and length were measured with micrometer calipers having a precision of 0.001 mm. For measuring the mass of the large samples, a balance with a precision of 0.1 g was employed. The mass of the small ones was measured with a balance having a precision

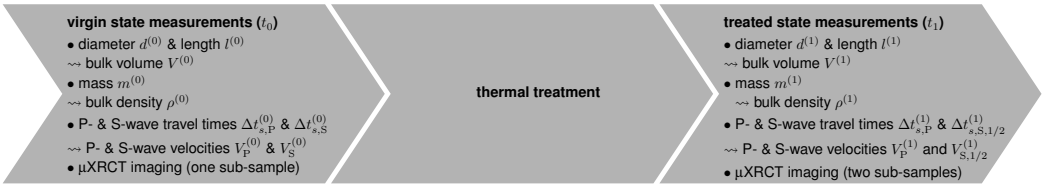

Figure 2. Measurement workflow.

of 0.001 g. All measurements were repeated three times and the subsequent steps were performed with the respective mean values.

The P- and S-wave velocities V_{P} and V_{S} in axial sample direction were determined using the ultrasonic through-transmission method. For measuring the P-wave velocities, two *Karl Deutsch S 12 HB 1* ultrasonic contact transducers were used, and for the S-wave velocities, a pair of *Olympus V153-RB* ones. Both transducer pairs are designed for an operating frequency of 1.0 MHz. The corresponding wavelengths are given by the ratio of the measured ultrasonic speeds (V_{P} or V_{S}) and the transducer frequency. For expected velocities between $6000\,\mathrm{m\,s^{-1}}$ to $1000\,\mathrm{m\,s^{-1}}$, the wavelengths should be in the range of 6 mm to 1 mm. Compared to the mean grain size diameter of Carrara marble in the range of 150 µm to 230 µm (Pieri et al., 2001; Fredrich et al., 1990), hence, we are in the large wavelength regime. Since the focus of this work is on the comparative characterization of different thermal treatments, velocity dispersion is not studied.

To identify a possible induced anisotropy, shear wave splitting was taken into account as done, for instance, in Peacock et al. (1994) and de Figueiredo et al. (2013). This means, that by polar measurements a potentially existing shear wave splitting was identified, and in the positive case, the velocities $V_{\mathrm{S},1}$ and $V_{\mathrm{S},2}$ of the faster and the slower traveling S-wave determined. To quantify the state of anisotropy, Thomsens's anisotropy parameter

$$\gamma = \frac{1}{2}\left(\frac{V_{\mathrm{S},1}^2}{V_{\mathrm{S},2}^2} - 1\right) \tag{1}$$

is introduced (Thomsen, 1986) and used in the same manner as in de Figueiredo et al. (2013). If no variation of the velocity V_{S_i} over the polarization angle φ_i can be observed, it follows $\gamma = 0$. This is typically for an isotropic homogeneous medium where no shear wave splitting occurs. Since the anisotropy effects of the reference samples (virgin state) were insignificant ($V_{\mathrm{S},1} \approx V_{\mathrm{S},2}$), isotropy was assumed in this state. Hence, for all remaining samples in the untreated state, the S-wave velocity was determined under an arbitrary angle.

To get an understanding how the microstructure is affected by the different thermal treatments, and in particular to observe the resulting differences between the slow and the fast cooling, µXRCT imaging was performed. The following three extreme conditions were considered: virgin state, 600slow, and 600fast. Since we are interested in expected small features, also the samples must be small enough to achieve suitable results. For this, from twin samples (diameter $d = 30\,\mathrm{mm}$, length $l = 80\,\mathrm{mm}$) which were subjected to exactly the same thermal treatment, core samples with a diameter of 5 mm and a length of about 10 mm were extracted and scanned. For the scans, the µXRCT system presented in Ruf and Steeb (2020c) was employed. Further details about the scan settings can be found in A2 of the Appendix. The resulting reconstructed data sets display physical volumes of $5.88\,\mathrm{mm} \times 5.88\,\mathrm{mm} \times 4.278\,\mathrm{mm}$ using a uniform voxel size of 2.0 µm ($2940 \times 2940 \times 2139$ voxel). Hence, the extracted samples

were be scanned over the entire diameter. In axial direction, it was focused on the middle part of the 10 mm long subsamples.

3 Results

The results of the absolute values for the determined density ρ, the P-wave velocity V_P as well as the S-wave velocity V_S, rather $V_{S,1}$ and $V_{S,2}$, of each sample, before and after the respective thermal treatment, can be found in Appendix C. Table C2 contains the results for the large samples and Table C3 for the small ones. From the descriptive statistic of the properties of the untreated samples, classified according to the used raw material blocks, it can be followed that they show only a slight variation within one block, cf. Table C1. Consequently, the three investigated Carrara marble blocks can be considered almost homogeneous. This substantiates the macroscopic homogeneous properties of Carrara marble listed in the introduction. Also, the variation in between the different used blocks is minor. Thus, the requirements of the aimed investigation are given.

To examine the influence of the different employed thermal treatments, in the following, the results are mainly presented as relative changes. This means that the absolute measured value differences between the two sample states are related to the corresponding measured values in the untreated sample. This eliminates the effect of minor variations in the absolute quantities. For details about the definition of the relative changes, see Appendix B. For the large sample geometry, the mean value and the standard deviation of the underlying three samples per thermal treatment are used as descriptive statistic measures. In all plots following, we employ red lines to refer to the slow cooling treatments and blue lines to refer to the fast cooling treatments. We start with the results of the large samples.

3.1 Large Samples

3.1.1 Bulk Volume and Bulk Density Change

In Figure 3(a) the relative change of the bulk volume and bulk density based on the underlying diameter, length, and mass measurements for the different thermal treatments is presented. For both groups of thermal treatments, a remaining bulk volume increase with an increasing peak temperature of the respective thermal treatment can be observed. The bulk volume increase is equivalent to a reduction of the bulk density. It already occurs significantly for the slow cooling and is strengthened in case of a fast cooling procedure. The error bars illustrate a greater variation of the results for the fast cooling procedure compared to the slow cooling procedure. This can be explained by the manual performed quenching protocol. The relationship just described also applies to the underlying relative changes of the diameter and length, shown in Figure 3(b). However, it is unexpected that the relative change of the length is systematically greater than the relative change of the diameter. Moreover, the difference increases with the maximum temperature.

3.1.2 Elastic Wave Propagation

Before considering the relative velocity changes, the possible anisotropic mechanical behavior perpendicular to the wave propagation direction is quantified. For this, for all samples, the shear wave speed under different polarization angles was measured, cf. section 2.2 and A1. The absolute measuring results against the polarization angle are exemplarily shown for one sample of each thermal treatment in Figure 4(a). There is a clear connection between the considered polarization angle and the resultant shear wave speed. Already the untreated sample shows slightly this behavior. This is evidence that the raw material is slightly anisotropic perpendicular to the wave

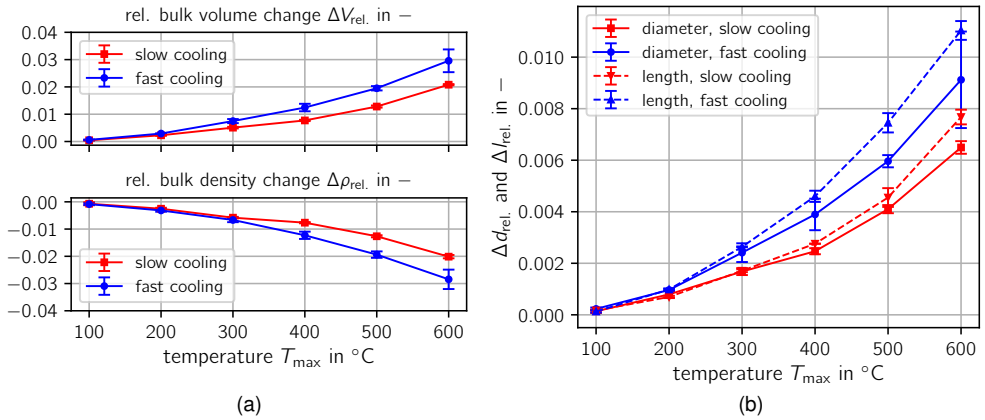

Figure 3. Remaining deformation under ambient conditions for the large samples after the applied thermal treatments. (a) Bulk volume and bulk density change. (b) Length and diameter change.

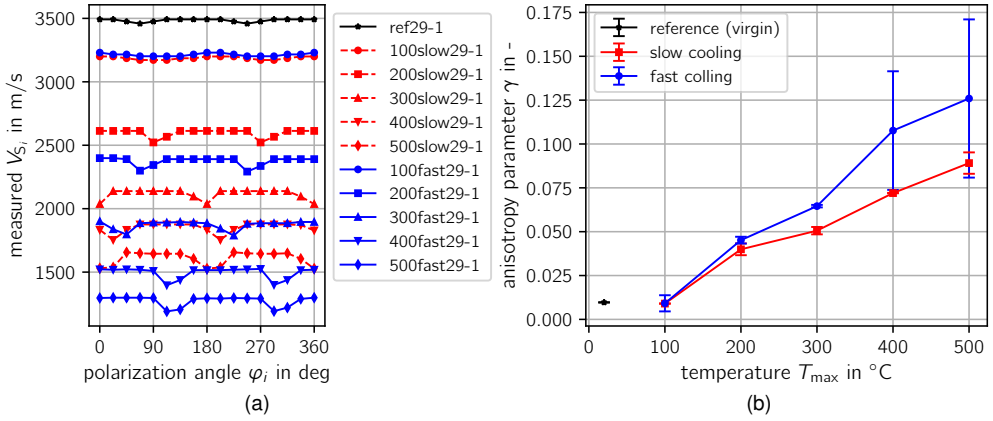

Figure 4. Influence of the applied thermal treatment on the shear wave velocity and the related shear wave splitting for the large samples. (a) Polar shear wave velocity measurements to determine the fast and the slow shear wave velocities. (b) Thomsen's anisotropy parameter γ based on the shear wave split.

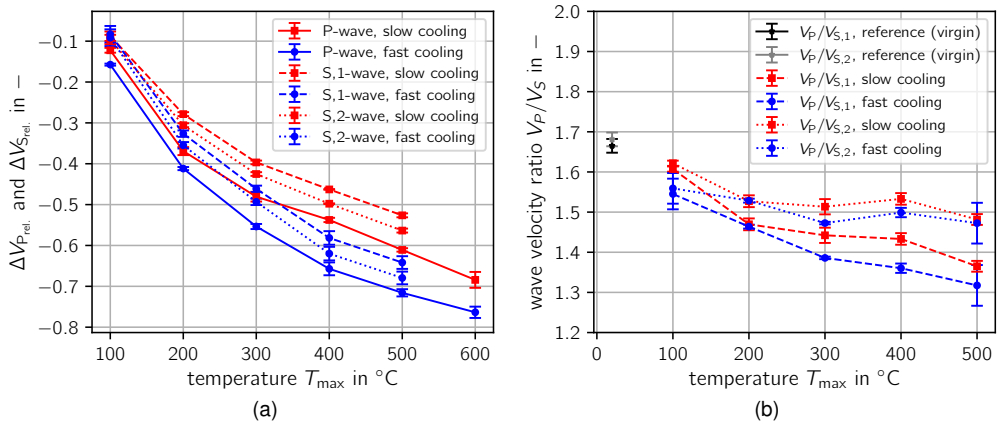

Figure 5. Influence of the applied thermal treatment on the P- and S-wave velocity for the large samples.

propagation direction. Since the anisotropy in the virgin state is comparatively low, this was neglected for the rest of the samples in the initial measurements. From the polar representation, we obtain the propagation velocities of the fast and the slow S-wave, $V_{S,1}$ and $V_{S,2}$, which are used to determine Thomsen's anisotropy parameter according to Eq. (1). The results are shown in Figure 4(b). Although the absolute difference between $V_{S,1}^{(1)}$ and $V_{S,2}^{(1)}$ does not increase significantly above a temperature of about 300 °C, cf. the corresponding maxima and minima in Figure 4(a), Thomsen's anisotropy parameter increases almost linearly over the entire temperature range. This is a result of the strong decrease of the wave velocities with the maximum applied temperature. Consequently, the almost isotropic mechanical properties of Carrara marble in the virgin state are not preserved after a thermal treatment with peak temperatures over 100 °C.

In Figure 5(a) the results of the relative P-wave velocity changes $V_{P,rel.}$ as well as the S-wave velocity changes $V_{S,1,rel.}$ and $V_{S,2,rel.}$ are presented. As already observed for the bulk volume/density change, there is a directly nonlinear correlation with the applied maximum temperature of the thermal treatment. Here, the greater the applied maximum temperature, the greater the reduction of the wave velocities. Over the entire temperature range, the P-wave propagation velocity decrease is slightly greater than the S-wave propagation velocity. For the highest applied temperature of 600 °C the P-wave speed reduction is about 76 % (68 %) in average for the fast cooling (slow cooling) method. This means that the absolute P-wave speed of about 5.8 km s^{-1} in the virgin sample drastically dropped to 1.4 km s^{-1} (1.8 km s^{-1}) after the corresponding heat treatment. The difference of the relative changes between the cooling methods is up to 350 °C depending on the peak temperature and above more or less constant. In Figure 5(b) the ratio of $V_P^{(1)}/V_{S,1}^{(1)}$ and $V_P^{(1)}/V_{S,2}^{(1)}$ over the maximum temperature is plotted. With increasing temperature, the ratio decreases for both groups and both velocity ratios. However, the decline over the temperature depends on the considered shear wave velocity. For the fast shear wave, the decline is significantly stronger. Since the ratio decreases with higher maximum temperature, it is increasingly more difficult and even impossible to determine reliably the arrival time of the shear waves. This explains why quantities utilizing the S-wave propagation velocities are only presented up to a maximum of 500 °C. In all cases, the standard deviation is low and for the slow cooled down samples again significantly less than for the fast cooled ones. The reasons are the same as already mentioned. The wavelengths are in the virgin state about 5.9 mm and 3.5 mm for the P-wave and the S-wave, respectively. Considering the extremes after the thermal treatments, they are reduced to 1.3 mm and 1.1 mm. For the higher peak temperatures, a signal gain of up to 40 dB for the P-wave measurements was required indicating a distinctive attenuation of the wave propagation. However, this observation is not investigated further within this work.

3.2 Influence of Sample Size

Up to now, all shown results were based on measurements of the large samples. To identify a potential size effect, in Figure 6 a comparison of the relative bulk volume change 6(a), the relative P-wave velocity change 6(b) as well as the relative S-wave velocity changes 6(c) and 6(d) for both sample sizes is shown. The bright lines refer to the large samples, and the dark dashed lines to the small ones. The courses of all lines largely coincide with the results of the large samples. The highest differences can be observed for the relative S-wave velocity changes. It is noted again that no statistics were considered for the small samples, and thus, only one sample per thermal treatment was investigated. Hence, the data of the small samples are not as smooth as for the large ones. The comparison of the relative bulk volume change does not allow any conclusions to be drawn regarding a size effect. The same holds for the relative change of the S-wave velocities due to an unsystematic variation of the data. However, a clear distinction can be observed for the P-wave velocity measurements. For the slow

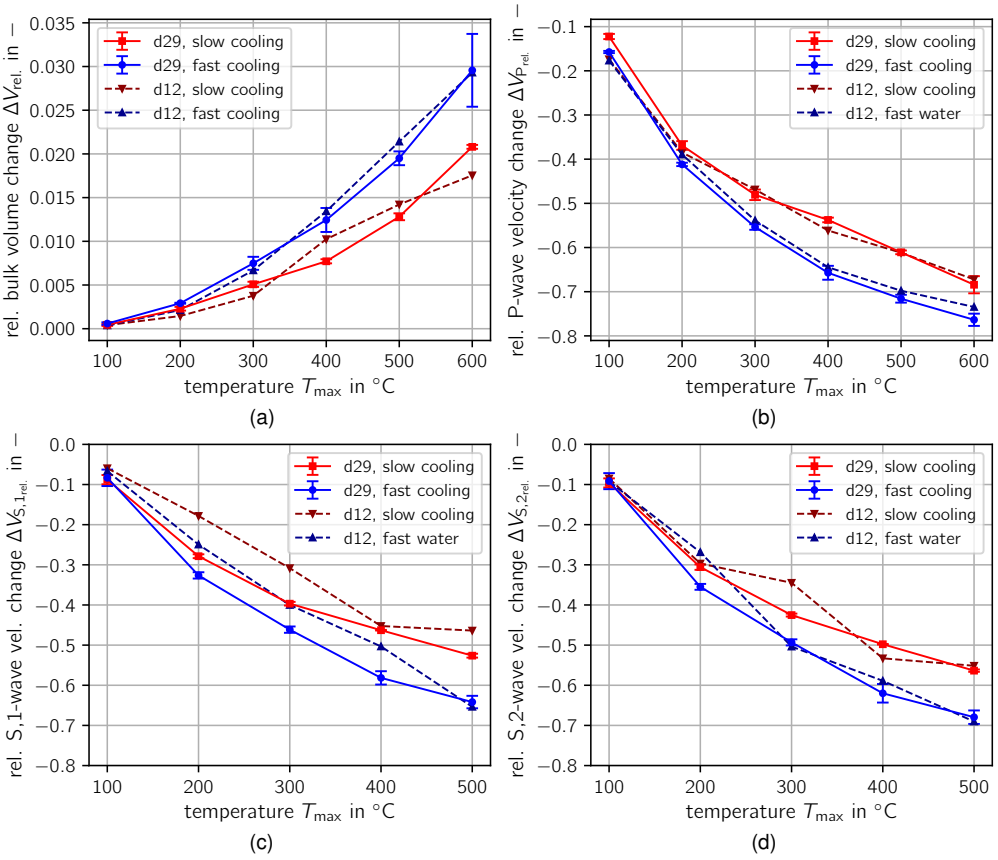

Figure 6. Comparison of the sample size influence on the effective properties for the different thermal treatments. (a) Relative bulk volume change. (b) Relative P-wave velocity change. (c) Relative S,1-wave velocity change. (d) Relative S,2-wave velocity change.

cooling procedure, we obtain nearly the same results independent of the sample size. However, for the fast cooling procedure, the drop of the propagation velocity for the small samples is for all thermal treatments slightly lower.

3.3 Correlation of Ultrasound Velocities with Bulk Volume Changes

So far, the measurement results of the ultrasonic velocity changes and the bulk volume changes were studied separately in dependency of the applied maximum temperature of the corresponding thermal treatment. To find out if there is a relationship between the bulk volume change and the wave velocity change, in Figure 7 all results are merged. Figure 7(a) and 7(b) display the relationship for the P-wave, Figure 7(c) and 7(d) for the S,1-wave and Figure 7(e) and 7(f) for the S,2-wave velocities, respectively. In this representation also the influence of the observed overshot for the two lowest maximum temperatures is eliminated, cf. Figure 1. From Figure 7(a), 7(c) and 7(e) follows, that there might exist a logarithmic relationship in all cases. To verify this, in Figure 7(b), 7(d) and 7(f) a semi-log scale for the bulk volume change is employed. Obviously, in all cases, all data points lie approximately on a straight line as indicated by a linear regression fit in the semi-log representation. This is evidence that regardless of the thermal treatment and the sample size, the relative wave propagation change is significantly driven by the initiated bulk volume change. This motivates to establish a model predicting the evolution of the acoustic velocity changes based

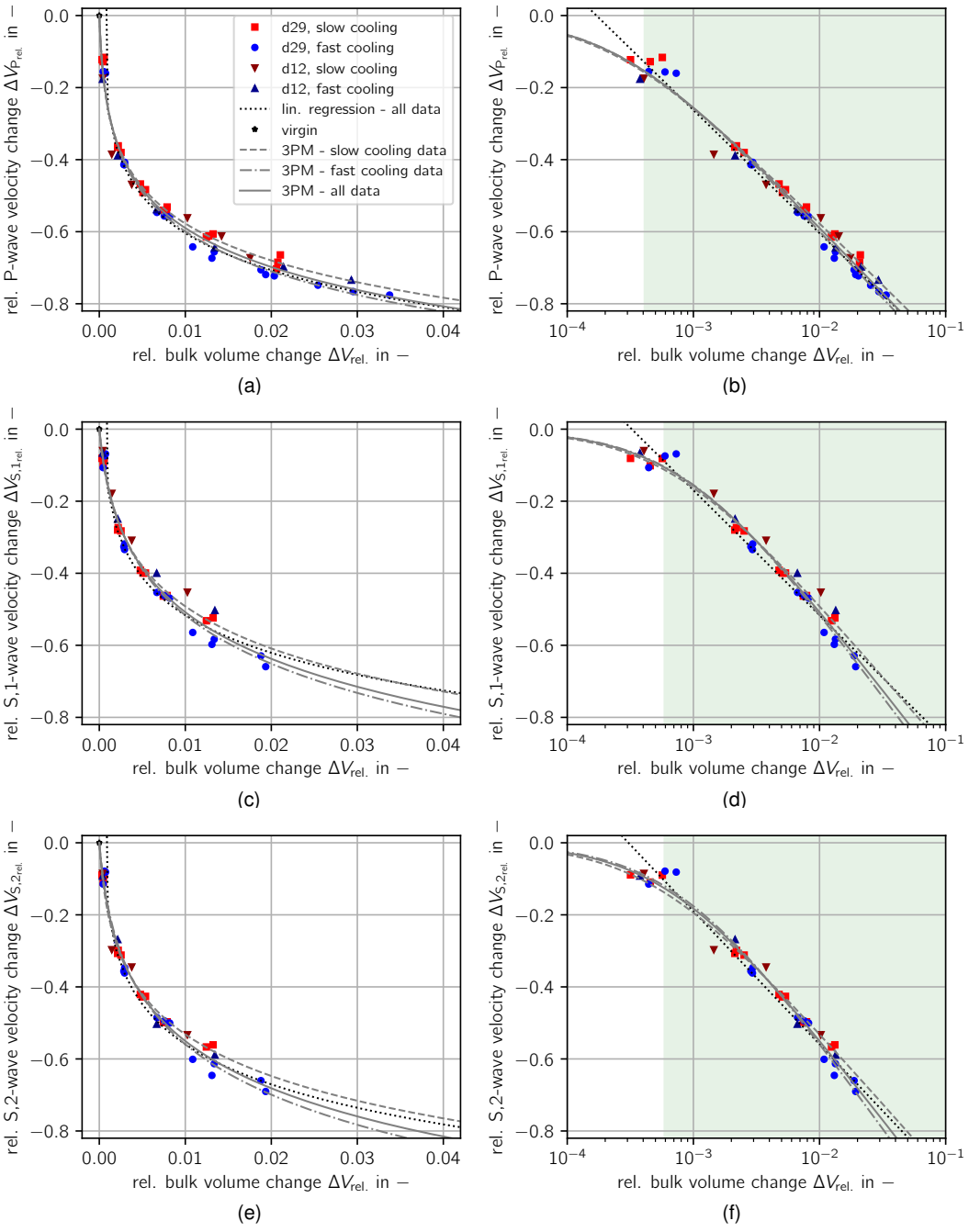

Figure 7. Relative wave propagation velocity change as a function of the relative bulk volume change and fitted models. (a), (b) Relative P-wave velocity change. (c), (d) Relative S,1-wave velocity change. (e), (f) Relative S,2-wave velocity change. The green area indicates the area, where the error between the "3PM - all data" and the "lin. regression - all data" is less than 15 %.

on the bulk volume changes. The fact that all data points in the semi-log plots lie approximately on a straight line motivates to employ a logarithmic model approach. Therefore, we propose for the relative P-wave and S-wave velocity changes ΔV_i with $i = \{\text{P, S,1, S,2}\}$, as a function of the relative bulk volume change $\Delta V_{\text{rel.}}$, following approach:

$$\Delta V_i(\Delta V_{\text{rel.}}) \quad = \quad m_i \log(\Delta V_{\text{rel.}} + c_i) + b_i \qquad \text{with} \qquad i = \{\text{P, S,1, S,2}\} \tag{2}$$

The parameters m_i, c_i and b_i are corresponding fit parameters. Therefore, we refer to this model as the 3-Parameter Model (3PM). The parameter c_i is needed to incorporate the untreated (virgin) sample state in the logarithmic formulation since no thermal treatment corresponds to no changes of the bulk volume and the ultrasonic velocities. This known data point cannot be incorporated in the pure linear regression fit in the semi-log space. However, to take into account the entire range starting at zero bulk volume change, the consideration of this point is essential. Otherwise, the model prediction for low bulk volume changes would lead to unexpected results. The parameter m_i describes the slope of the resulting straight line in the semi-log representation when shifted by c_i and the parameter b_i the interception point with the vertical axis. The parameter identification was consequently constrained by the requirement to include the fixed point $(0, 0)$. For higher bulk volume changes a slightly but systemically separation of the data points depending on the cooling procedure can be observed, cf. Figure 7. Therefore, several fits were performed employing the following data sets: slow cooling, fast cooling, and all data points. The model parameters were determined using a classical least-squares approach. The resulting parameters together with the coefficients of determination R_i^2 for the different regressions are summarized in Table 1. Also the determined parameters of the linear regression fits in the semi-log space are listed where the parameter c_i vanishes ($c_i = 0$).

Table 1. Identified model parameters for the fits shown in Figure 7.

P-wave fits	m_{P}	b_{P}	c_{P}	R^2_{P}
3PM - slow cooling data	−0.346 305	−1.266 638	0.000 220	0.982 194
3PM - fast cooling data	−0.375 409	−1.345 850	0.000 260	0.991 076
3PM - all data	−0.365 760	−1.317 489	0.000 250	0.983 690
lin. regression - all data; no (0,0)	−0.341 478	−1.286 921	0.000 000	0.988 046
S,1-wave fits	$m_{\text{S,1}}$	$b_{\text{S,1}}$	$c_{\text{S,1}}$	$R^2_{\text{S,1}}$
3PM - slow cooling data	−0.407 075	−1.294 683	0.000 660	0.985 975
3PM - fast cooling data	−0.476 778	−1.452 151	0.000 900	0.980 624
3PM - all data	−0.455 469	−1.403 265	0.000 830	0.979 391
lin. regression - all data; no (0,0)	−0.346 923	−1.210 285	0.000 000	0.967 163
S,2-wave fits	$m_{\text{S,2}}$	$b_{\text{S,2}}$	$c_{\text{S,2}}$	$R^2_{\text{S,2}}$
3PM - slow cooling data	−0.397 186	−1.318 166	0.000 480	0.987 261
3PM - fast cooling data	−0.490 494	−1.524 408	0.000 780	0.987 143
3PM - all data	−0.455 621	−1.449 084	0.000 660	0.983 177
lin. regression - all data; no (0,0)	−0.369 207	−1.297 795	0.000 000	0.976 782

As can be followed from Figure 7 in combination with the coefficients of determination, the optimized models can reproduce the underlying data well. Using the specific data sets results in a slightly improved fit than employing all data points. This can be observed in the plots as well as in the related coefficients of determination. Up to a bulk volume change of about 1.0 %, there is no significant difference of the fits in

between the cooling procedures. For the border data points in terms of the maximum bulk volume change, the relative error by using the model fitted for all data points instead of the specif one is less than 2.5 % for the P-wave model and less than 4.6 % for the S,1/S,2-wave models. In Figure 7(b), 7(d) and 7(f) the region is highlighted, where the relative error between the 3PM and the linear regression is less than 15 %. This corresponds to relative bulk volume changes greater than 4.1×10^{-4} (0.041 %) for the P-wave velocity changes and 5.9×10^{-4} (0.059 %) for the S-wave velocity changes. For reasons of simplicity, in this regime also a prediction based on the linear regression fit can be justifiable.

Based on the models given by Eq. (2) and the related optimized parameters in Table 1, the absolute values of the corresponding P- and S-wave velocities $V_{\mathrm{P}}^{(1)}$ as well as $V_{\mathrm{S},1}^{(1)}$ and $V_{\mathrm{S},2}^{(2)}$ (abbreviated $V_{\mathrm{S},1/2}^{(1)}$) can be determined by

$$V_{\mathrm{P}}^{(1)}(\Delta V_{\mathrm{rel.}}) = V_{\mathrm{P}}^{(0)} \left[m_{\mathrm{P}} \log(\Delta V_{\mathrm{rel.}} + c_{\mathrm{P}}) + b_{\mathrm{P}} + 1 \right] \quad \text{and} \tag{3}$$

$$V_{\mathrm{S},1/2}^{(1)}(\Delta V_{\mathrm{rel.}}) = V_{\mathrm{S}}^{(0)} \left[m_{\mathrm{S},1/2} \log(\Delta V_{\mathrm{rel.}} + c_{\mathrm{S},1/2}) + b_{\mathrm{S},1/2} + 1 \right] , \tag{4}$$

employing the ultrasound velocities of the untreated samples and the relative bulk volume change. In combination with the associated modified bulk volume density

$$\rho^{(1)}(\Delta V_{\mathrm{rel.}}) = \frac{\rho^{(0)}}{\Delta V_{\mathrm{rel.}} + 1} , \tag{5}$$

an estimation of the elastic moduli can be done, cf. e.g. Mavko et al. (2009). The required underlying quantities in the untreated state needed for this are given by $V_{\mathrm{P}}^{(0)} = 5871\,\mathrm{m\,s^{-1}}$, $V_{\mathrm{S}}^{(0)} = 3519\,\mathrm{m\,s^{-1}}$ and $\rho^{(0)} = 2700\,\mathrm{kg\,m^{-3}}$ using the mean values of all investigated samples, see Table C1. Since the relation between the wave propagation velocities and the dynamic elastic moduli is typically based on an isotropic material behavior, their application must be treated with caution. Further, only one wave propagation direction was evaluated and consequently, no statement over the overall anisotropic material behavior can be made.

3.4 Change of Microstructure

In Figure 8 the acquired µXRCT data sets of the three extreme cases are condensed by the use of three different representative cutting planes (xy-, zx- and yz-plane). The full three 3D data sets of the slow, Figure 8(b), and the fast, Figure 8(c), cooled down samples can be found in Ruf and Steeb (2020b, 2020a). In all cases, the bright gray area represents the calcite phase of the Carrara marble. The surrounding dark gray represents air. In all scans some usual ring artifacts in the center are present. Figure 8(a) exhibits the extremely homogeneous properties of Carrara marble in the virgin state. Apart from few inclusions and few very small pores the whole sample appears completely homogeneous. No microcracks or similar signs of damage can be identified. Due to the underlying physical principle, it is not possible to detect grain boundaries, as they do not show any difference in the attenuation coefficient. Figure 8(b) and Figure 8(c) exhibit the inner structure after the thermal treatment at the highest investigated maximum temperature of 600 °C and a subsequent slow and fast cooling. In both cases, a nearly homogeneous crack-network can be seen that crosses the entire data sets. The contrast of the crack network in Figure 8(c) is higher, which is a result of the greater mean crack aperture in combination with the given spatial resolution of the employed system. Even if the crack networks seem to be homogeneous, individual cracks can be identified which exhibit a lager aperture than the average ones. This can be observed especially in the zx- and the yz-section plane.

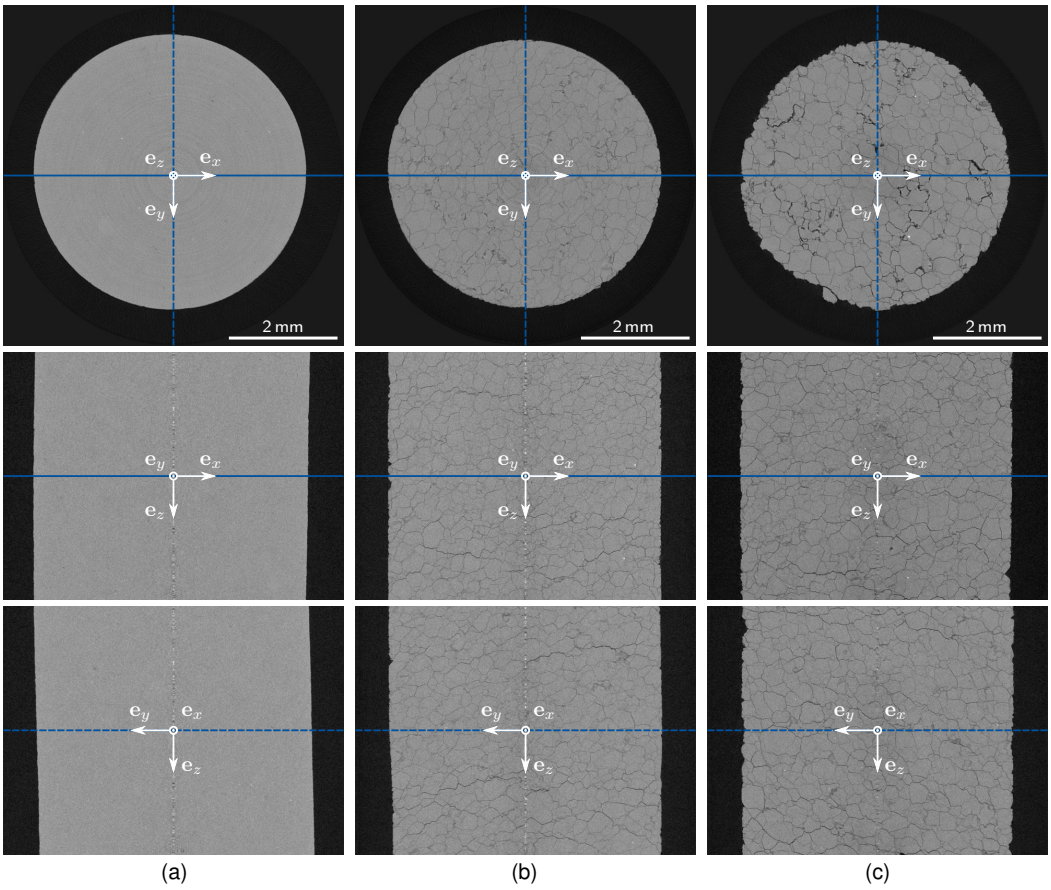

Figure 8. Representative images (xy-, zx- and yz-section plane) from three different µXRCT data sets showing the inner structure of Carrara marble in different conditions. (a) Virgin state. (b) $T_{\max} = 600\,°C$ and slow cooling (c) $T_{\max} = 600\,°C$ and fast cooling. The underlying data sets of (b) and (c) can be found in Ruf and Steeb (2020a, 2020b); https://doi.org/10.18419/darus-754 and https://doi.org/10.18419/darus-639; licensed under a Creative Commons Attribution (CC BY) license.

4 Discussion

The µXRCT data sets in Figure 8 show clearly the effects of the thermal treatments on the microstructure. Independent of the applied cooling method, a crack network was formed crossing the whole sample. The strictly monotonous and smooth curves in Figure 3 in combination with the µXRCT images signal clearly that the bulk volume increase for both thermal treatments is the result of the newly created crack volume and not of irreversible phase transformations. Pimienta et al. (2019) inferred the same based on their investigations on thermally treated Carrara marble slowly cooled down. In this work, additionally, the bulk volume change was compared with the pore volume change (effective porosity) based on pycnometer measurements of the whole samples. Good agreement was shown for maximum temperatures up to 400 °C. For higher temperatures, a non-systematical variation could be observed. This could be due to the examination of only one sample per thermal treatment. If we suppose that no additional remaining phase transformations occur (calcite to aragonite or vaterite, cf. e.g. Ševčík et al. (2017)), the bulk volume increase is identical to the increase of the total porosity. When we qualitatively compare Figure 8(b) with Figure 8(c), the

density of cracks, meaning the crack length per unit area in 2D (Kranz, 1983; Moore & Lockner, 1995), respectively the crack area per unit volume in 3D, is roughly the same. However, the mean crack aspect-ratio, defined by the ratio of the crack aperture to the crack length, in Figure 8(c) is obviously greater. This explains the bulk volume difference of about 0.9 percent point in Figure 3(a) for $T_{\max} = 600\,^{\circ}\mathrm{C}$, which is about 42 % greater in case of the fast cooling. Consequently, there have to be two different mechanisms affecting the resulting crack volume. The question could arise why the µXRCT data sets are only evaluated in a qualitatively way and not further quantified, for instance, to determine the crack density and the mean crack aperture. This is because, even if the cracks are easy to recognize visually, it is still extremely difficult to reliably segment them, cf. Lee et al. (2021). To exclude this kind of error source, it was deliberately avoided in this work. In µXRCT imaging it is generally challenging to resolve features with an extreme length/width aspect ratio which is typically for microcracks. On the one side, a high spatial system resolution is required to achieve accurate information about the crack aperture. On the other side, a large field of view is mandatory to have a representative volume. Especially the crack aperture in the range of a few micrometers cannot quantitatively be determined in a reliable way since the gray-scale contrast is too low due to the limited spatial resolution of the employed system. If the cracks are completely closed or have a very small aperture, it is expected that they should not be visible at all due to the typical noise in the scan data sets. This is also a further reason why samples for the µXRCT scans were used, which were treated with the highest maximum temperatures. The problem mentioned is also causal, why samples treated by lower maximum temperature were not scanned. For these, the crack opening is too small to obtain reliable information. To further investigate the influence of the crack density and crack aspect ratio leading to the same total crack porosity, it is advisable to employ also other methods such as classical microscopy, but with the disadvantage of obtaining only 2D information.

From investigations on the physical weathering of Carrara marble in the lower temperature range ($T_{\max.} \leq 80\,^{\circ}\mathrm{C}$), it is known that the anisotropic thermal expansion of the randomly oriented calcite grains and the resulting misfit strains are responsible for the initiation of cracks during the heating-up process (Siegesmund et al., 2000; Shushakova et al., 2012). If the crack closure is hindered during the cooling process, further cracks can be formed (Shushakova et al., 2012) or existing ones remain open. This becomes understandable if the thermal expansion of calcite is considered in more detail. Calcite has a trigonal crystal system and exhibits a temperature depending positive thermal expansion coefficient $\alpha_{\parallel}$ along and a negative thermal expansion coefficient $\alpha_{\perp}$ perpendicular to the optic axis (Srinivasan, 1955; Rao et al., 1968; Dove et al., 2005). In Rao et al. (1968) equations for the thermal expansion coefficients for the temperature range from 28 °C to 524 °C were derived from experimental measurements. According to this, $\alpha_{\parallel}$ is in the range of $25.16 \times 10^{-6}\,\mathrm{K}^{-1}$ to $32.40 \times 10^{-6}\,\mathrm{K}^{-1}$, and $\alpha_{\perp}$ in the range of $-3.68 \times 10^{-6}\,\mathrm{K}^{-1}$ to $-4.95 \times 10^{-6}\,\mathrm{K}^{-1}$, which points out, that high stresses between differently oriented grains during the heating-up phase are inevitable. Since the difference between $\alpha_{\parallel}$ and $\alpha_{\perp}$ is increasing with the temperature, the mechanism known from physical weathering of Carrara marble is even heightened for higher peak temperatures. For a more detailed illustration of the mechanisms of thermal induced microcracks it is referred to Fredrich and Wong (1986), Clarke (1980) and Evans and Clarke (1980). Since the calcite grain boundaries cannot be visualized by the employed imaging method, it is unclear whether the formed cracks are inter- or intragranular ones. Based on the crack initiation mechanism and the known typical mean grain sizes of Carrara marble from the literature, in the range of ≈150 µm (Pieri et al., 2001) to ≈230 µm (Fredrich et al., 1990), it is supposed that the major ones are intergranular cracks. However, this depends strongly on the grain-boundary toughness and the relation to other rock fabric properties as investigated by Shushakova et al. (2012) for temperatures between ±50 °C. Therefore, this remains an open question. The crack initiation mechanism as a result of the anisotropy thermal expansion of the

calcite grains, also explains the correlation with the applied maximum temperature and is in accordance with the results of Pimienta et al. (2019). The resulting remaining deformation is also known as residual strain and occurs even for temperature changes of only 20 K to 50 K, cf. Siegesmund et al. (2000) and the therein cited literature. This explains why already for the lowest considered maximum temperature of 100 °C a relatively small bulk volume increase results in a significant change of the ultrasonic velocity. The detected difference between the relative diameter and length change in Figure 3(b) can only be the result of an underlying preferential oriented texture, which in general should be weak or non-existent for Carrara marble (Siegesmund et al., 2000) but is not uncommon, cf. Sheremeti-Kabashi and Snethlage (2000).

The mechanism described above explains the crack initiation process in the case of both groups of thermal treatments since it is in principle independent of the cooling procedure. However, in the case of a subsequent fast cooling, there is a second mechanism that amplifies the first one in terms of the generated crack volume as obvious from the bulk volume measurements. The underlying mechanism is well known as thermal shock and frequently happens, for instance, as an undesired effect in ceramics, cf. Kingery (1955). Here, the rapid cooling results in temperature gradients leading to a non-uniform strain distribution within the sample. If the local resulting stresses exceed the material strength, cracks are formed or existing ones are propagating or opened. Whereas the first mechanism depends strongly on the material and the underlying microstructure, the second one is always present and can also be used to initiate cracks in non-crystalline materials like borosilicate glass (Ougier-Simonin et al., 2010, 2011). The effect of thermal quenching correlates with the difference between the maximum employed temperature and the temperature of the water basin. This explains the increasing difference in terms of the bulk volume or density with increasing maximum temperature for the two different thermal treatment groups. Further, this effect depends on the sample size since this affects the achievable temperature gradients within the sample (Kingery, 1955).

For better understanding of the size effect, we roughly estimate the maximum resulting temperature difference $\Delta T_{\max}$ within the two employed sample sizes ($d = 29\,\mathrm{mm}$ and $d = 12\,\mathrm{mm}$). For this, we consider an endless cylinder with Robin boundary conditions during the non-stationary cooling and neglect the effects on the sample tips. To solve the initial boundary value problem, we use the analytical solution in cylindrical coordinates, cf. e.g. Marek and Nitsche (2019). The maximum possible temperature difference is given by the difference between the temperature on the sample surface T_{surface} and the core T_{center}, $\Delta T_{\max} = T_{\mathrm{center}} - T_{\mathrm{surface}}$ holds. We consider the cooling from the initial sample temperature $T_0 = 600\,^{\circ}\mathrm{C}$ in a water basin with temperature $T_\infty = 20\,^{\circ}\mathrm{C}$ and employ as heat transfer coefficient $h = 8000\,\mathrm{W\,m^{-2}\,K^{-1}}$. For the required material properties, we employ average values for Carrara marble covering the examined temperature range, which are in general depending on the temperature. For the density $\rho = 2700\,\mathrm{kg\,m^{-3}}$, for the specific heat capacity $c_p = 1000\,\mathrm{J\,kg^{-1}\,K^{-1}}$ and for the thermal conductivity $k = 1.5\,\mathrm{W\,m^{-1}\,K^{-1}}$ were set, cf. Merriman et al. (2018). The evolving temperatures (T_{center} and T_{surface}) over time are shown in Figure 9(a) and the resulting maximum temperature difference $\Delta T_{\max}$ in Figure 9(b). It is obvious, that the resulting maximum temperature difference $\Delta T_{\max}$ is significantly higher in the case of the larger sample diameter. Consequently, higher strain differences inside the sample arise, and potentially, more cracks are created, or existing ones are opened. Both explain the slightly higher reduction of the P-wave velocities for the large samples in Figure 6(b). Although the size effect cannot be observed in terms of the relative bulk volume variation and the relative S-wave velocity changes, cf. Figure 6(a), 6(c) and 6(d), the much more reliable P-wave measurements are evident that this effect exists. In general, the reliable determination of the S-wave velocity becomes more difficult with increasing crack porosity. The reason for this is the almost linear decreasing P- to S-wave velocity ratio with increasing maximum

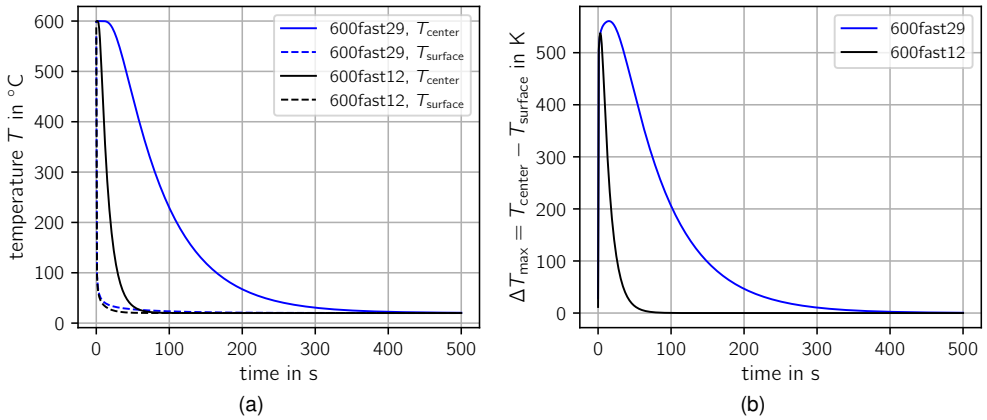

Figure 9. Illustration of the influence of the sample diameter on the resulting temperature distribution during fast cooling. Estimation based on the analytical solution for an endless cylinder geometry with Robin boundary conditions, cf. e.g. Marek and Nitsche (2019). Initial temperature $T_0 = 600\,°C$, environment temperature (water basin) $T_\infty = 20\,°C$, heat transfer coefficient $h = 8000\,W\,m^{-2}\,K^{-1}$. Underlying (averaged) material properties for Carrara marble: thermal conductivity $k = 1.5\,W\,m^{-1}\,K^{-1}$, density $\rho = 2700\,kg\,m^{-3}$ and specific heat capacity $c_p = 1000\,J\,kg^{-1}\,K^{-1}$, cf. Merriman et al. (2018).

temperature of the subsequent thermal treatment, cf. Figure 5(b). Since the transmitted pulse of the S-wave transducer always includes P-wave portions, the first arrival of the S-wave is superimposed more and more by parts of the P-wave arriving before. For a physical interpretation of the velocity ratio V_P/V_S, we consider the ideal case of isotropic material behavior. In this case, the ratio of the compression modulus K and the shear modulus μ is given by $K/\mu = (V_P/V_S)^2 - 4/3$, cf. e.g. Mavko et al. (2009). Consequently, a reduction of V_P/V_S means that the compressive stiffness decreases proportionally more than the shear stiffness. This statement also holds for the thermally treated samples, although they cannot considered as isotropic material. From the S-wave measurements, it can be concluded that a low to non-existent elastic anisotropy in the untreated sample state will be amplified or initiated by thermal treatments and may need attention. In particular, the application of theories based on assumptions about isotropic material behavior must be used with caution, e.g. the conversation from wave propagation velocities to dynamic elastic moduli. Employing Thomsen's anisotropy parameter for the quantification of the elastic anisotropy in one direction, an approximately linear increase with the used maximum temperature results, which is steeper for the fast cooling. That implicates that the crack aspect ratio has a strong influence on the anisotropy. Due to the increasing rate of anisotropy with the maximum temperature, it is advisable to consider not only one direction for the characterization.

The necessary amplification of the receiver transducer signal of up to 40 dB for the samples treated at higher maximum temperatures is evident that a drastic wave attenuation occurs. From the 3D microstructure visualization, it is obvious that scattering on the crack surfaces and absorption due to friction should be the causal mechanisms. The different required signal gain for the P-wave (up to 40 dB) and the S-wave (up to 20 dB) measurements with increasing relative bulk volume change agrees with the observed sensitivity of the P-wave and the S-wave velocity change, cf. Figure 7. This can be explained by the underlying difference in the kinematics of the two waves.

Independent of the specimen size as well as the underlying thermal treatment, Figure 7 shows a clearly logarithmic correlation between the relative bulk volume increase, identical to the initiated crack porosity, and the relative change of the wave propagation velocities. The drastic drop of the velocities already arise for comparable small crack porosities of less than one percent initiated by thermal treatments with less than 400 °C maximum temperature. Even a moderate temperature of 100 °C creates already numerous irreversible microcracks within the sample, as the wave velocity reduction shows. As mentioned in section 3.3, for higher relative bulk volume changes a separation of the underlying data points of the slow and the fast cooled down samples can be observed. This means that for an identical crack porosity the velocities are systematically slightly different. This can be well observed, for instance, on the samples that have a crack porosity of approximately 2.0 % after the respective thermal treatment. To obtain this crack porosity, either heating to 600 °C has to be performed, followed by slow cooling or heating up to 500 °C with subsequent fast cooling. Since the crack porosity is nearly identical, the different effect on the velocity change can only be explained with different values of the crack density and the mean crack aspect ratio. Coming back to the example, it is supposed that the slowly cooled down sample has a higher crack density but a lower mean crack aspect ratio since a higher maximum temperature was employed. This hypothesis is based on the consideration that the heating-up phase is primarily responsible for the crack initiation and the fast cooling just holds the cracks more or less open. The latter is to be understood in such a way that due to the nonuniform strain field as a result of the fast cooling the mismatch between the individual grains is amplified. Besides, it is supposed that in a sample that already contains numerous cracks, it is difficult to build up stresses by thermal shock large enough to initiate completely new cracks. Therefore, probably crack propagation is the dominating mechanism. However, since the differences are minor, in a good approximation the crack porosity increase can be employed as characterizing and simply measurable macroscopic quantity to estimate how the wave propagation is affected. In micro-mechanics, the challenge is to find appropriate microstructural parameters that determine the value of the effective physical properties, cf. Guéguen and Kachanov (2011) and Kachanov and Sevostianov (2013). For dry Carrara marble with cracks initiated by thermal treatments, the increase of the crack porosity, which is the same as the relative bulk volume increase, is an appropriate microstructural parameter to predict the wave velocity change under ambient conditions. In other words, the observed stiffness decrease correlating with the reduction of the wave propagation velocities with increasing crack volume, contains the information about the generated microcracks. Consequently, the measured effective properties may be interpreted as a mixture of the calcite grain phase with unchanged properties (identical to the effective properties in the untreated state) and the stiffness of the cracks.

5 Summary and Conclusions

A systematic study and comparison about the effects of two groups of thermal treatments, distinguishing in the cooling conditions, slow and fast cooling, was carried out for Bianco Carrara marble. As effective properties, the bulk volume, the bulk density, and the P- and S-wave ultrasonic velocities before and after the thermal treatment were determined. For the latter, also shear wave splitting was taken into account. For all measurements, an increase of the bulk volume corresponding with a decrease of the bulk density and a decrease of the wave velocities with increasing maximum temperature of the employed thermal treatments could be observed. Growing shear wave splitting with the employed maximum temperature indicated an increase of anisotropy. For the samples which were subjected to fast cooling, the results were systematically amplified compared to the slowly cooled samples. Based on μXRCT scans, the microstructure changes as a result of the employed thermal treatments compared to the virgin state were visualized for the extreme cases. For both, a nearly homoge-

nous network of microcracks was formed, which explains the bulk volume increase. Therefore, the relative increase of the bulk volume is supposed to be identical to the initiated crack porosity. From the µXRCT scans, it was obvious that the generated crack network mainly differs in the mean crack aspect-ratio. Following the literature, it could be shown that the dominating microfracture generation happens already during the heating-up phase due to anisotropic thermal expansion of the calcite grains. If fast cooling instead of slow cooling is applied, the crack porosity can be significantly increased. It is supposed that mainly the mean crack aspect-ratio is influenced by the fast cooling and not the crack density. It could be shown, that a logarithm relationship between the relative change of the ultrasonic velocities and the relative bulk volume increase exists. The latter is identical to the initiated crack porosity by thermal treatment. This relationship also explains why the fast cooling compared to the slow cooling, holding all other factors fixed, had only a minor influence on the wave propagation velocity but a major on the bulk volume. From the resulting data base, models were derived by employing a logarithm model approach with three parameters. The parameters were determined using least squares method. A slightly systematic difference dependent on the cooling method could be identified. Here it was supposed that for the same crack porosity, a different composition of the crack density and the mean crack aspect ratio is causal. Since the impact on the relative change of the wave velocities is insignificant, the macroscopical measurable relative bulk volume increase after a thermal treatment can be used to predict the relative change of the wave velocities. The proposed model approach should be applicable in general for Bianco Carrara marble with customized parameters as they are influenced by the exact rock fabric. If values of the absolute quantities of the ultrasonic velocities in the virgin sample state exist, a prediction of the absolute quantities after the thermal treatment based on the relative bulk volume increase can be performed. The resulting ultrasonic velocities can be used to derive other quantities as, for instance, the dynamic moduli. However, attention must be paid on potential initiated elastic anisotropy as a result of the thermal treatment. In this case, theories that assume isotropic material behavior are no longer valid or restricted.

To initiate the same crack porosity, both thermal treatments are capable up to a certain maximum crack porosity with approximately the same influence on the macroscopic properties. Using slow cooling is more advisable since no dependency on the sample size exists. Further, slow cooling shows significantly less variation in the resulting measurement data and is, therefore, more deterministic. The only reason to employ a fast cooling for Carrara marble is when a higher crack porosity is required than can be realized by slow cooling. Depending on the microstructure, there are materials where no fracturing during the heating up occurs. For these kinds of materials, fast cooling (thermal shock) is the only possibility to initiate microcracks by a thermal treatment. We suppose that the qualitative results found are also transferable to other crystalline rocks within certain limits.

Appendix A Experimental Characterization Details

A1 Ultrasonic Velocities

In the through-transmission technique, there are two probes, one on either side of the sample, whereby one transmits a pulse while the other receives the pulse after a certain travel time. With the current sample length l (here $l^{(0)}$ or $l^{(1)}$) and the related travel time Δt_s of the pulse within the sample, the wave propagation velocities

$$V_{\mathrm{P}} = \frac{l}{\Delta t_{s,\mathrm{P}}} \quad \text{and} \quad V_{\mathrm{S}} = \frac{l}{\Delta t_{s,\mathrm{S}}} \tag{A1}$$

can be derived. The employed experimental setup is shown in Figure A1. For the coupling of the transducers to the sample surface, an adequate couplant was used.

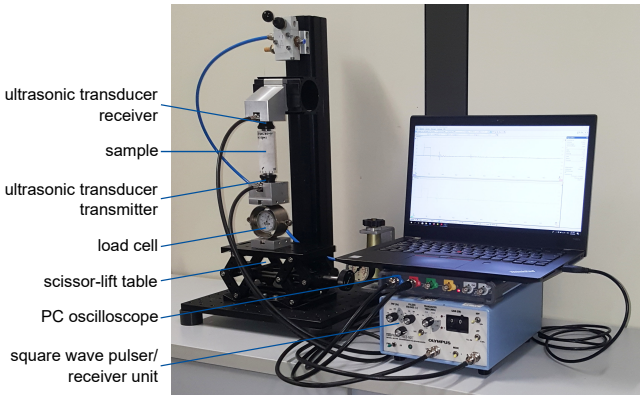

Figure A1. Photograph of the experimental setup for the determination of the wave velocities using the ultrasonic through-transmission method.

All measurements were performed under an identical contact pressure of 0.25 MPa. The related force was adjusted using a scissors-lift table and a mechanical load cell. As ultrasonic square wave pulser/receiver, the *Olympus-Panametrics 5077PR* unit in combination with the PC oscilloscope *PicoScope 5444B* was employed. For all samples an amplified square wave of 100 V with a repetition frequency of 100 Hz was set. The signals were recorded with a resolution of 15 bit and a sampling rate of 125 MS/s. To reduce random noise, stacking of 32 signals was consequently performed. No additional signal gain was needed for all measurements before the thermal treatments. In contrast, for the thermally treated samples, especially at higher max. temperatures ($\geq 400\,^{\circ}\mathrm{C}$), an additional signal gain was indispensable. This was set as low as possible. To determine the respective first arrival points of the emitted pulses, a similar systematic approach as in Jacobsson and Kjell (2017) was used. This involves following steps:

1. Low pass filtering of the raw signal for noise reduction.
2. Vertical signal offset correction.
3. Determination of the local signal minima and maxima.
4. Search for the first signal peak which also satisfies absolute or/and relative criteria.
5. Definition of two points at 20 % and 80 % of the first peak amplitude which are used to reconstruct a secant line.
6. Intersection of the secant line with the time axis gives the first arrival point.

The resulting time Δt is larger by the system time $\Delta t_{\mathrm{sys.}}$ than the pure travel time within the sample Δt_{s}, $\Delta t_{\mathrm{s}} = \Delta t - \Delta t_{\mathrm{sys.}}$ holds. The system times $\Delta t_{\mathrm{sys.}}$ were experimentally determined for the two setups using two aluminum standards with a different length (l_1 and l_2) made out of the same semi-finished product. Since in both standards the speed of sound must be equal, the system time follows from the two measured time periods Δt_1 and Δt_2:

$$\frac{l_1}{\Delta t_1 - \Delta t_{\mathrm{sys.}}} = \frac{l_2}{\Delta t_2 - \Delta t_{\mathrm{sys.}}} \quad \rightsquigarrow \quad \Delta t_{\mathrm{sys.}} = \frac{l_2 \Delta t_1 - l_1 \Delta t_2}{l_2 - l_1} \tag{A2}$$

To achieve a plane wave approximation, the basic requirement of ultrasonic measurement is that the sample diameter is much larger than the transducer diameter (Zhang et al., 2002). It is noted, that this is fulfilled for the large sample geometry, however, not for the small one. For the latter, the size ratio is about 1.0. Zhang et al. (2002) studied experimentally the influence of different sample and transducer size ratios on longitudinal waves for ceramic samples. For the here given ratio of ≈ 1.0, the influence

was minor. For the relative changes we are mainly interested in, the impact should be even smaller.

For measuring the velocity $V_{\mathrm{S},1}$ and $V_{\mathrm{S},2}$, the opposite S-wave transducers were aligned and fixed according to their polarization direction. Subsequently, the sample was examined with respect to the polarization direction given by the orientation of the transducers. This was done by rotating the sample to different angle positions φ_i. The acquired receiver transducer signal is equal to the vector sum of the two shear waves in the direction of its orientation. If the polarization of the transducers is parallel to one of the two directions of the split shear waves, the shear wave is not split. A plot of the corresponding velocities V_{S_i} over the examined angles φ_i should result in a smooth $\cos(2\,\varphi_i)$ curve if the angle increments $\Delta\varphi$ are chosen small enough. Based on this, the propagation velocities of the two split shear waves are given by $V_{\mathrm{S},1} = \max(V_{\mathrm{S}_i})$ and $V_{\mathrm{S},2} = \min(V_{\mathrm{S}_i})$ with the corresponding polarization angles $\varphi_{0,1}$ and $\varphi_{0,2}$, whereas $\varphi_{0,2} = \varphi_{0,1} + \pi/2$ holds. It is important to note that the value pairs in between the maximum and the minimum velocities have no physical meaning. Since one full period corresponds to the range $\varphi = \pi$, investigating the interval $[0°, 180°]$ for the polarization angle φ_i is sufficient. However, to cross-check the velocities, we measured the large samples over the entire circumference, $\varphi_i \in [0°, 360°]$ in increments of $\Delta\varphi = 22.5°$. The small samples were measured for $\varphi_i \in [0°, 180°]$ in identical increments of $\Delta\varphi = 22.5°$.

A2 Micro X-ray Computed Tomography Imaging

For the µXRCT scans, an in-house modular built-up cone beam µXRCT system with a maximum spatial resolution of about 50 lp/mm at 10 % of Modulation Transfer Function (MTF) was employed. A detailed description of the system used can be found in Ruf and Steeb (2020c). All scans were performed using the same geometric magnification of about 24.75. The X-ray tube voltage was set to 80 kV with a tube flux of 100 µA. The beam spectrum was additionally modified by a 0.5 mm thick Al-filter. As detector a Shad-o-Box 6K HS with a CsI scintillator option from Teledyne DALSA Inc., Waterloo, Ontario, Canada was used. In total, 1800 projections from 5 different slightly shifted detector positions with an exposure time of 3000 µs were recorded and stitched to final 1800 enhanced projections as explained in Ruf and Steeb (2020c). The reconstruction was performed using the filtered back projection algorithm within the commercial software Octopus Reconstruction, Version 8.9.4-64 bit (Vlassenbroeck et al., 2007). The corresponding voxel size of the reconstructed data sets is in all three cases about 2.0 µm. The resulting volumes have a dimension of $2940 \times 2940 \times 2139$ voxel corresponding to $5.88\,\mathrm{mm} \times 5.88\,\mathrm{mm} \times 4.278\,\mathrm{mm}$. In the presented data sets noise reduction filtering was deliberately not applied yet. Compared to classical optical microscopy or scanning electron microscope providing only a 2D information, µXRCT makes possible to visualize the internal 3D structure in a noninvasive way. However, the underlying physical principle only allows a feature detection if there is a distinction in the attenuation coefficient, cf. Carmignato et al. (2018) and Stock (2008). The brighter the shade of gray in the reconstructed volumes, the higher the X-ray attenuation which correlates with the material density and vice versa.

Appendix B Definition of Relative Changes

The relative change of the sample diameter d, length l and bulk volume V is defined by

$$\Delta d_{\mathrm{rel.}} = \frac{d^{(1)}}{d^{(0)}} - 1\,, \qquad \Delta l_{\mathrm{rel.}} = \frac{l^{(1)}}{l^{(0)}} - 1\,, \qquad \text{and} \qquad \Delta V_{\mathrm{rel.}} = \frac{V^{(1)}}{V^{(0)}} - 1 = \frac{l^{(1)} {d^{(1)}}^2}{l^{(0)} {d^{(0)}}^2} - 1\,. \tag{B1}$$

The relative change of the bulk density ρ follows by

$$\Delta\rho_{\mathrm{rel.}} = \frac{\rho^{(1)}}{\rho^{(0)}} - 1 = \frac{m^{(1)}}{V^{(1)}} \frac{V^{(0)}}{m^{(0)}} - 1\,. \tag{B2}$$

with the sample mass m. Due to the conservation of mass, the mass should be identical for both sample states, $m = m^{(0)} = m^{(1)}$. If this is fulfilled, verified accordingly by measuring twice, the relations

$$\Delta\rho_{\text{rel.}} = \frac{V^{(0)}}{V^{(1)}} - 1 \quad \text{and} \quad \Delta V_{\text{rel.}} = \frac{\rho^{(0)}}{\rho^{(1)}} - 1 \tag{B3}$$

hold. Therefore, with the absolute quantities for the density given in Table C2 and Table C3, the relative change of the density $\Delta\rho_{\text{rel.}}$ and the relative change of the bulk volume $\Delta V_{\text{rel.}}$ can be determined.

The relative changes for the P- and S-wave velocities are defined as

$$\Delta V_{\text{P}_{\text{rel.}}} = \frac{V_{\text{P}}^{(1)}}{V_{\text{P}}^{(0)}} - 1 \quad \text{and} \quad \Delta V_{\text{S}_{\text{rel.}}} = \frac{V_{\text{S}}^{(1)}}{V_{\text{S}}^{(0)}} - 1\,. \tag{B4}$$

In case of shear wave splitting, the relative changes of the velocity of the faster and the slower shear waves are consequently defined by

$$\Delta V_{\text{S},1_{\text{rel.}}} = \frac{V_{\text{S},1}^{(1)}}{V_{\text{S},1}^{(0)}} - 1 \quad \text{and} \quad \Delta V_{\text{S},2_{\text{rel.}}} = \frac{V_{\text{S},2}^{(1)}}{V_{\text{S},2}^{(0)}} - 1\,. \tag{B5}$$

If isotropy in the virgin state is assumed ($V_{\text{S},1}^{(0)} \approx V_{\text{S},2}^{(0)}$), then $V_{\text{S},1}^{(0)}$ and $V_{\text{S},2}^{(0)}$ are respectively replaced by $V_{\text{S}}^{(0)}$.

Appendix C Absolute Measurement Data

The descriptive statistics of the samples in the virgin state, classified according to the used raw material blocks, are given in Table C1. The absolute determined quantities for bulk density as well as velocities are given in Table C2 for the large samples and for the small ones in Table C3. For the measurements before the thermal treatment the superscript "(0)" and after the thermal treatment the superscript "(1)" is used.

Table C1. Descriptive statistic properties (mean value and standard deviation) of the dry, untreated samples, classified according to the used raw material blocks. Measurements performed under ambient conditions.

block	samples	$\rho^{(0)}$ [g/cm^3]	$V_{\text{P}}^{(0)}$ [m/s]	$V_{\text{S}}^{(0)}$ [m/s]
80 mm block a	100x29-x, 200x29-x, 300x29-x	2.705 ± 0.0018	5995 ± 42.0	3578 ± 17.6
80 mm block b	400x29-x, 500x29-x, 600x29-x, ref-x	2.699 ± 0.0024	$5787 \pm 37.4.6$	3483 ± 19.8
40 mm block	xx12-1	2.694 ± 0.0024	5836 ± 102.8	3498 ± 50.1
all blocks	all	2.700 ± 0.0048	5871 ± 111.2	3519 ± 52.3

Acknowledgments

MR and HS acknowledge funding from the German Science Foundation (DFG) through the project STE 969/13-1. The µXRCT images (reconstructed data sets, projection data sets and metadata) of the thermally treated Carrara marble samples and all other measurement data (geometry, mass and ultrasonic measurements) that support the findings of this study are openly available in the Data Repository of the University of Stuttgart (DaRUS) at `https://doi.org/10.18419/darus-754` (Ruf & Steeb, 2020b), `https://doi.org/10.18419/darus-682` (Ruf & Steeb, 2020a), and `https://doi.org/10.18419/darus-1862` (Ruf & Steeb, 2021).

Table C2. Absolute measured properties of dry, large samples (diameter $d = 29\,\mathrm{mm}$, length $l = 72.5\,\mathrm{mm}$). Measurements performed under ambient conditions.

sample name	$\rho^{(0)}$ [g/cm^3]	$\rho^{(1)}$ [g/cm^3]	$V_\mathrm{P}^{(0)}$ [m/s]	$V_\mathrm{P}^{(1)}$ [m/s]	$V_{\mathrm{S},1}^{(0)}$ [m/s]	$V_{\mathrm{S},2}^{(0)}$ [m/s]	$V_{\mathrm{S},1}^{(1)}$ [m/s]	$V_{\mathrm{S},2}^{(1)}$ [m/s]
slow cooled samples								
100slow29-1	2.706	2.704	5924	5165	3560		3200	3172
100slow29-2	2.699	2.698	5972	5239	3560		3272	3242
100slow29-3	2.705	2.702	5975	5280	3579		3288	3258
200slow29-1	2.704	2.698	6072	3876	3595		2613	2522
200slow29-2	2.704	2.697	6020	3731	3577		2566	2462
200slow29-3	2.706	2.698	5972	3791	3577		2576	2479
300slow29-1	2.704	2.688	5978	3043	3561		2139	2037
300slow29-2	2.705	2.688	5972	3085	3560		2138	2042
300slow29-3	2.706	2.691	5972	3180	3578		2177	2071
400slow29-1	2.702	2.681	5805	2719	3486		1876	1754
400slow29-2	2.702	2.682	5808	2668	3484		1870	1749
400slow29-3	2.698	2.677	5805	2667	3493		1874	1752
500slow29-1	2.701	2.665	5790	2279	3479		1656	1527
500slow29-2	2.700	2.667	5787	2231	3482		1630	1508
500slow29-3	2.701	2.667	5806	2254	3499		1669	1529
600slow29-1	2.701	2.645	5831	1956	3509		-	-
600slow29-2	2.701	2.646	5805	1830	3487		-	-
600slow29-3	2.697	2.644	5662	1679	3454		-	-
fast cooled samples								
100fast29-1	2.707	2.704	6077	5132	3616		3230	3202
100fast29-2	2.705	2.703	6024	5059	3579		3333	3288
100fast29-3	2.705	2.703	6078	5126	3622		3353	3337
200fast29-1	2.707	2.699	5973	3500	3561		2398	2292
200fast29-2	2.705	2.697	5972	3499	3578		2382	2285
200fast29-3	2.706	2.696	6020	3567	3577		2438	2336
300fast29-1	2.705	2.688	5973	2640	3578		1900	1788
300fast29-2	2.705	2.689	5973	2709	3578		1956	1842
300fast29-3	2.706	2.686	5974	2650	3561		1916	1802
400fast29-1	2.699	2.670	5808	2079	3500		1525	1396
400fast29-2	2.700	2.664	5799	1995	3492		1456	1351
400fast29-3	2.698	2.663	5762	1881	3468		1396	1229
500fast29-1	2.700	2.650	5783	1701	3503		1298	1190
500fast29-2	2.698	2.647	5779	1623	3474		1184	1076
500fast29-3	2.696	2.640	5767	1599	3467		1259	1081
600fast29-1	2.691	2.624	5789	1455	3480		-	-
600fast29-2	2.698	2.612	5728	1284	3435		-	-
600fast29-3	2.696	2.619	5767	1348	3468		-	-
thermally untreated reference samples								
ref29-1	2.698	-	5774	-	3492	3459	-	-
ref29-2	2.699	-	5825	-	3458	3425	-	-
ref29-3	2.701	-	5840	-	3524	3490	-	-

Table C3. Absolute measured properties of dry, small samples (diameter $d = 12\,\text{mm}$, length $l = 30\,\text{mm}$). Measurements performed under ambient conditions.

sample name	$\rho^{(0)}$ [g/cm^3]	$\rho^{(1)}$ [g/cm^3]	$V_\text{P}^{(0)}$ [m/s]	$V_\text{P}^{(1)}$ [m/s]	$V_{\text{S},1}^{(0)}$ [m/s]	$V_{\text{S},2}^{(0)}$ [m/s]	$V_{\text{S},1}^{(1)}$ [m/s]	$V_{\text{S},2}^{(1)}$ [m/s]
slow cooled samples								
100slow12-1	2.692	2.690	6019	4972	3540	3330	3240	
200slow12-1	2.696	2.691	5802	3568	3432	2820	2413	
300slow12-1	2.695	2.683	5737	3049	3452	2388	2262	
400slow12-1	2.697	2.670	5838	2560	3504	1919	1637	
500slow12-1	2.691	2.653	5927	2301	3554	1905	1594	
600slow12-1	2.690	2.642	5847	1916	3523	-	-	
fast cooled samples								
100fast12-1	2.694	2.692	5916	4870	3522	3288	3197	
200fast12-1	2.697	2.690	5884	3593	3491	2620	2553	
300fast12-1	2.697	2.680	5903	2723	3488	2093	1731	
400fast12-1	2.693	2.656	5604	1991	3416	1697	1404	
500fast12-1	2.696	2.638	5705	1724	3443	1192	1066	
600fast12-1	2.693	2.612	5838	1550	3508	-	-	
thermally untreated reference samples								
ref12-1	2.691	-	5846	-	3598	-	-	

References

Anders, M. H., Laubach, S. E., & Scholz, C. H. (2014). Microfractures: A review. *Journal of Structural Geology*, *69*, 377–394. doi: 10.1016/j.jsg.2014.05.011

Arena, A., Delle Piane, C., & Sarout, J. (2014). A new computational approach to cracks quantification from 2D image analysis: Application to micro-cracks description in rocks. *Computers & Geosciences*, *66*, 106–120. doi: 10.1016/j.cageo.2014.01.007

Carmignato, S., Dewulf, W., & Leach, R. (Eds.). (2018). *Industrial X-Ray Computed Tomography*. Springer International Publishing. doi: 10.1007/978-3-319-59573-3

Clarke, D. R. (1980). Microfracture in brittle solids resulting from anisotropic shape changes. *Acta Metallurgica*, *28*(7), 913–924. doi: 10.1016/0001-6160(80)90107-8

de Figueiredo, J. J. S., Schleicher, J., Stewart, R. R., Dayur, N., Omoboya, B., Wiley, R., & William, A. (2013). Shear wave anisotropy from aligned inclusions: Ultrasonic frequency dependence of velocity and attenuation. *Geophysical Journal International*, *193*(1), 475–488. doi: 10.1093/gji/ggs130

Delle Piane, C., Arena, A., Sarout, J., Esteban, L., & Cazes, E. (2015). Micro-crack enhanced permeability in tight rocks: An experimental and microstructural study. *Tectonophysics*, *665*, 149–156. doi: 10.1016/j.tecto.2015.10.001

Delle Piane, C., & Burlini, L. (2008). Influence of strain history on the mechanical and micro-fabric evolution of calcite rocks: Insights from torsion experiments. *Swiss Journal of Geosciences*, *101*(2), 361–375.

Dove, M. T., Swainson, I. P., Powell, B. M., & Tennant, D. C. (2005). Neutron powder diffraction study of the orientational order–disorder phase transition in calcite, CaCO3. *Physics and Chemistry of Minerals*, *32*(7), 493–503. doi: 10.1007/s00269-005-0026-1

El Boudani, M., Wilkie-Chancellier, N., Martinez, L., Hébert, R., Rolland, O., Forst,

S., ... Serfaty, S. (2015a). Marble ageing characterization by acoustic waves. *Physics Procedia*, *70*, 222–226. doi: 10.1016/j.phpro.2015.08.140

El Boudani, M., Wilkie-Chancellier, N., Martinez, L., Hébert, R., Rolland, O., Forst, S., ... Serfaty, S. (2015b). Marble characterization by ultrasonic methods. *Procedia Earth and Planetary Science*, *15*, 249–256. doi: 10.1016/j.proeps.2015.08.061

Evans, A. G., & Clarke, D. R. (1980). Residual stresses and microcracking induced by thermal contraction inhomogeneity. In *Thermal Stresses in Severe Environments* (pp. 629–648). Springer US. doi: 10.1007/978-1-4613-3156-8_39

Fredrich, J. T., Evans, B., & Wong, T. (1990). Effect of grain size on brittle and semibrittle strength: Implications for micromechanical modelling of failure in compression. *Journal of Geophysical Research*, *95*(B7), 10907. doi: 10.1029/jb095ib07p10907

Fredrich, J. T., & Wong, T. (1986). Micromechanics of thermally induced cracking in three crustal rocks. *Journal of Geophysical Research: Solid Earth*, *91*(B12), 12743–12764. doi: 10.1029/jb091ib12p12743

Guéguen, Y., & Kachanov, M. (2011). Effective elastic properties of cracked rocks – an overview. In *Mechanics of Crustal Rocks* (pp. 73–125). Springer Vienna. doi: 10.1007/978-3-7091-0939-7_3

Howarth, D. F., Adamson, W. R., & Berndt, J. R. (1986). Correlation of model tunnel boring and drilling machine performances with rock properties. *International Journal of Rock Mechanics and Mining Sciences & Geomechanics Abstracts*, *23*(2), 171–175. doi: 10.1016/0148-9062(86)90344-x

Jacobsson, L., & Kjell, G. (2017). *Measurement of P- and S-wave velocity in material using ultrasonics* (Tech. Rep.). RISE Research Institutes of Sweden.

Kachanov, M., & Sevostianov, I. (Eds.). (2013). *Effective Properties of Heterogeneous Materials*. Springer Netherlands. doi: 10.1007/978-94-007-5715-8

Kandula, N., Cordonnier, B., Boller, E., Weiss, J., Dysthe, D. K., & Renard, F. (2019). Dynamics of microscale precursors during brittle compressive failure in Carrara marble. *Journal of Geophysical Research: Solid Earth*, *124*(6), 6121–6139. doi: 10.1029/2019jb017381

Kingery, W. D. (1955). Factors affecting thermal stress resistance of ceramic materials. *Journal of the American Ceramic Society*, *38*(1), 3–15. doi: 10.1111/j.1151-2916.1955.tb14545.x

Kranz, R. L. (1983). Microcracks in rocks: A review. *Tectonophysics*, *100*(1-3), 449–480. doi: 10.1016/0040-1951(83)90198-1

Lee, D., Karadimitriou, N., Ruf, M., & Steeb, H. (2021). *Detecting micro fractures with x-ray computed tomography.*

Lissa, S., Ruf, M., Steeb, H., & Quintal, B. (2021). Digital rock physics applied to squirt flow. *Geophysics*, 1–40. doi: 10.1190/geo2020-0731.1

Marek, R., & Nitsche, K. (2019). *Praxis der Wärmeübertragung.* Hanser Fachbuchverlag.

Mavko, G., Mukerji, T., & Dvorkin, J. (2009). *The Rock Physics Handbook – Tools for Seismic Analysis of Porous Media* (2nd ed.). Cambridge University Press.

Merriman, J. D., Hofmeister, A. M., Roy, D. J., & Whittington, A. G. (2018). Temperature-dependent thermal transport properties of carbonate minerals and rocks. *Geosphere*, *14*(4), 1961–1987. doi: 10.1130/ges01581.1

Moore, D., & Lockner, D. (1995). The role of microcracking in shear-fracture propagation in granite. *Journal of Structural Geology*, *17*(1), 95–114. doi: 10.1016/0191-8141(94)e0018-t

Ougier-Simonin, A., Fortin, J., Guéguen, Y., Schubnel, A., & Bouyer, F. (2010). Cracks in glass under triaxial conditions. *International Journal of Engineering Science*, *49*(1), 105–121. doi: 10.1016/j.ijengsci.2010.06.026

Ougier-Simonin, A., Guéguen, Y., Fortin, J., Schubnel, A., & Bouyer, F. (2011). Permeability and elastic properties of cracked glass under pressure. *Journal of*

Geophysical Research, *116*(B7). doi: 10.1029/2010jb008077

Peacock, S., McCann, C., Sothcott, J., & Astin, T. (1994). Seismic velocities in fractured rocks: An experimental verification of Hudson's theory. *Geophysical Prospecting*, *42*(1), 27–80. doi: 10.1111/j.1365-2478.1994.tb00193.x

Pieri, M., Burlini, L., Kunze, K., Stretton, I., & Olgaard, D. L. (2001). Rheological and microstructural evolution of Carrara marble with high shear strain: Results from high temperature torsion experiments. *Journal of Structural Geology*, *23*(9), 1393 - 1413. doi: 10.1016/S0191-8141(01)00006-2

Pimienta, L., Orellana, L. F., & Violay, M. (2019). Variations in elastic and electrical properties of crustal rocks with varying degree of microfracturation. *Journal of Geophysical Research: Solid Earth*, *124*(7), 6376–6396. doi: 10.1029/2019jb017339

Ramez, M. R. H., & Murrell, S. A. F. (1964). A petrofabric analysis of Carrara marble. *International Journal of Rock Mechanics and Mining Sciences & Geomechanics Abstracts*, *1*(2), 217–229. doi: 10.1016/0148-9062(64)90028-2

Rao, K. V. K., Naidu, S. V. N., & Murthy, K. S. (1968). Precision lattice parameters and thermal expansion of calcite. *Journal of Physics and Chemistry of Solids*, *29*(2), 245–248. doi: 10.1016/0022-3697(68)90068-1

Rodriguez-Navarro, C., Ruiz-Agudo, E., Luque, A., Rodriguez-Navarro, A. B., & Ortega-Huertas, M. (2009). Thermal decomposition of calcite: Mechanisms of formation and textural evolution of CaO nanocrystals. *American Mineralogist*, *94*(4), 578–593. doi: 10.2138/am.2009.3021

Ruf, M., & Steeb, H. (2020a). *micro-XRCT data set of Carrara marble with artificially created crack network: fast cooling down from 600° C.* DaRUS. doi: 10.18419/darus-682

Ruf, M., & Steeb, H. (2020b). *micro-XRCT data set of Carrara marble with artificially created crack network: slow cooling down from 600° C.* DaRUS. doi: 10.18419/darus-754

Ruf, M., & Steeb, H. (2020c). An open, modular, and flexible micro X-ray computed tomography system for research. *Review of Scientific Instruments*, *91*(11), 113102. doi: 10.1063/5.0019541

Ruf, M., & Steeb, H. (2021). *Effects of thermal treatment on acoustic waves in Carrara marble: measurement data.* DaRUS. doi: 10.18419/darus-71862

Sarout, J., Cazes, E., Delle Piane, C., Arena, A., & Esteban, L. (2017, aug). Stress-dependent permeability and wave dispersion in tight cracked rocks: Experimental validation of simple effective medium models. *Journal of Geophysical Research: Solid Earth*, *122*(8), 6180–6201. doi: 10.1002/2017jb014147

Schubnel, A., Benson, P. M., Thompson, B. D., Hazzard, J. F., & Young, R. P. (2006). Quantifying damage, saturation and anisotropy in cracked rocks by inverting elastic wave velocities. *Pure and Applied Geophysics*, *163*(5-6), 947–973. doi: 10.1007/s00024-006-0061-y

Schubnel, A., Walker, E., Thompson, B. D., Fortin, J., Guéguen, Y., & Young, R. P. (2006). Transient creep, aseismic damage and slow failure in Carrara marble deformed across the brittle-ductile transition. *Geophysical Research Letters*, *33*(17). doi: 10.1029/2006gl026619

Ševčík, R., Šašek, P., & Viani, A. (2017, dec). Physical and nanomechanical properties of the synthetic anhydrous crystalline CaCO3 polymorphs: vaterite, aragonite and calcite. *Journal of Materials Science*, *53*(6), 4022–4033. doi: 10.1007/s10853-017-1884-x

Sheremeti-Kabashi, F., & Snethlage, R. (2000). Determination of structural anisotropy of Carrara marble with ultrasonic measurements. In *Proceedings of the 9th international congress on deterioration and conservation of stone* (pp. 247–253). Elsevier. doi: 10.1016/b978-044450517-0/50106-9

Shushakova, V., Fuller, E. R., & Siegesmund, S. (2012). Microcracking in calcite and dolomite marble: microstructural influences and effects on properties. *Environ-*

mental Earth Sciences, *69*(4), 1263–1279. doi: 10.1007/s12665-012-1995-2

Siegesmund, S., Ullemeyer, K., Weiss, T., & Tschegg, E. K. (2000). Physical weathering of marbles caused by anisotropic thermal expansion. *International Journal of Earth Sciences*, *89*(1), 170–182. doi: 10.1007/s005310050324

Srinivasan, R. (1955). The thermal expansion of calcite from room temperature up to 400°C. *Proceedings of the Indian Academy of Sciences - Section A*, *42*(2), 81–85. doi: 10.1007/bf03053495

Stock, S. R. (2008). *MicroComputed Tomography: Methodology and Applications*. CRC Press.

Thomsen, L. (1986). Weak elastic anisotropy. *Geophysics*, *51*(10), 1954–1966. doi: 10.1190/1.1442051

Vlassenbroeck, J., Dierick, M., Masschaele, B., Cnudde, V., Van Hoorebeke, L., & Jacobs, P. (2007). Software tools for quantification of X-ray microtomography at the UGCT. *Nuclear Instruments and Methods in Physics Research Section A: Accelerators, Spectrometers, Detectors and Associated Equipment*, *580*(1), 442–445. doi: 10.1016/j.nima.2007.05.073

Zhang, R., Jiang, B., & Cao, W. (2002). Influence of sample size on ultrasonic phase velocity measurements in piezoelectric ceramics. *Journal of Applied Physics*, *91*(12), 10194. doi: 10.1063/1.1479754